2014

The Crustal Thickness of West Antarctica

Julien A. Chaput
Universite Joseph Fourier (Grenoble I)

Richard C. Aster
New Mexico Institute of Mining and Technology

Audrey D. Huerta
Central Washington University, audrey.huerta@cwu.edu

X. Sun
Washington University in St. Louis

Andrew Lloyd
Washington University in St. Louis

See next page for additional authors

Recommended Citation

Chaput, J. et al. (2014). The crustal thickness of West Antarctica. *Journal of Geophysical Research: Solid Earth 119*(1), 378-395. DOI: 10.1002/2013JB010642

Authors
Julien A. Chaput, Richard C. Aster, Audrey D. Huerta, X. Sun, Andrew Lloyd, Douglas A. Wiens, Andrew Nyblade, Sridhar Anandakrishnan, J. Paul Winberry, and Terry Wilson

JOURNAL OF GEOPHYSICAL RESEARCH: SOLID EARTH, VOL. 119, 378–395, doi:10.1002/2013JB010642, 2014

The crustal thickness of West Antarctica

J. Chaput,[1] R. C. Aster,[2,3] A. Huerta,[4] X. Sun,[5,6] A. Lloyd,[5] D. Wiens,[5] A. Nyblade,[7] S. Anandakrishnan,[7] J. P. Winberry,[4] and T. Wilson[8]

Received 30 August 2013; revised 25 November 2013; accepted 26 November 2013; published 8 January 2014.

[1] P-to-S receiver functions (PRFs) from the Polar Earth Observing Network (POLENET) GPS and seismic leg of POLENET spanning West Antarctica and the Transantarctic Mountains deployment of seismographic stations provide new estimates of crustal thickness across West Antarctica, including the West Antarctic Rift System (WARS), Marie Byrd Land (MBL) dome, and the Transantarctic Mountains (TAM) margin. We show that complications arising from ice sheet multiples can be effectively managed and further information concerning low-velocity subglacial sediment thickness may be determined, via top-down utilization of synthetic receiver function models. We combine shallow structure constraints with the response of deeper layers using a regularized Markov chain Monte Carlo methodology to constrain bulk crustal properties. Crustal thickness estimates range from 17.0 ± 4 km at Fishtail Point in the western WARS to 45 ± 5 km at Lonewolf Nunataks in the TAM. Symmetric regions of crustal thinning observed in a transect deployment across the West Antarctic Ice Sheet correlate with deep subice basins, consistent with pure shear crustal necking under past localized extension. Subglacial sediment deposit thicknesses generally correlate with trough/dome expectations, with the thickest inferred subice low-velocity sediment estimated as ∼ 0.4 km within the Bentley Subglacial Trench. Inverted PRFs from this study and other published crustal estimates are combined with ambient noise surface wave constraints to generate a crustal thickness map for West Antarctica south of 75°S. Observations are consistent with isostatic crustal compensation across the central WARS but indicate significant mantle compensation across the TAM, Ellsworth Block, MBL dome, and eastern and western sectors of thinnest WARS crust, consistent with low density and likely dynamic, low-viscosity high-temperature mantle.

Citation: Chaput, J., R. C. Aster, A. Huerta, X. Sun, A. Lloyd, D. Wiens, A. Nyblade, S. Anandakrishnan, J. P. Winberry, and T. Wilson (2014), The crustal thickness of West Antarctica, *J. Geophys. Res. Solid Earth*, *119*, 378–395, doi:10.1002/2013JB010642.

1. Introduction

1.1. The West Antarctic Rift System

[2] The West Antarctic Rift System (WARS; Figure 1) is a broad extended region, comparable in scale to the western North American Basin and Range province [e.g., *Behrendt*, 1999]. The WARS is distinguished among Earth's continental rift systems in being associated with low intraplate rates of deformation [*Wilson et al.*, 2011], low seismicity [*Winberry and Anandakrishnan*, 2003; *Reading*, 2007], generally low subice elevations (e.g., hundreds of meters above sea level after accounting for ice sheet loading [*Wilson and Luyendyk*, 2009]), thin crust [*Winberry and Anandakrishnan*, 2004], low-viscosity mantle [*Wiens et al.*, 2012], and (at least in some regions) high heat flow in excess of 120 mW/m^2 [*Clow et al.*, 2012], all of which significantly influence West Antarctic Ice Sheet (WAIS) dynamics and history [*Pollard et al.*, 2005]. To better understand these aspects of West Antarctic tectonics and their contributions to ice sheet processes, the POLENET-ANET project (the West Antarctic and Transantarctic Mountains portion of the Polar Earth Observing Network), funded as part of the International Polar Year (IPY), deployed a seismographic and geodetic network of unprecedented duration and scale across the WAIS/Transantarctic Mountains (TAM) region. A notable feature of the WARS is the presence of the extraordinarily deep ice-filled grabens of the Byrd Subglacial Basin and Bentley Subglacial Trough (the lowest points on Earth's

Additional supporting information may be found in the online version of this article.

[1]ISTERRE, Université Joseph Fourier, Grenoble, France.
[2]Department of Earth and Environmental Science, New Mexico Institute of Mining and Technology, Socorro, New Mexico, USA.
[3]Geosciences Department, Colorado State University, Fort Collins, Colorado, USA.
[4]Department of Geological Sciences, Central Washington University, Ellensburg, Washington, USA.
[5]Department of Earth and Planetary Sciences, Washington University, St. Louis, Missouri, USA.
[6]State Key Laboratory of Isotope Geochemistry, Guangzhou Institute of Geochemistry, Chinese Academy of Sciences, Guangzhou, China.
[7]Department of Geosciences, Pennsylvania State University, University Park, Pennsylvania, USA.
[8]School of Earth Sciences, Ohio State University, Columbus, Ohio, USA.

Corresponding author: J. Chaput, ISTERRE, Université Joseph Fourier, Grenoble I, BP 53, 38041 Grenoble CEDEX 9, France. (jchaput@ees.nmt.edu)

2169-9313/14/10.1002/2013JB010642

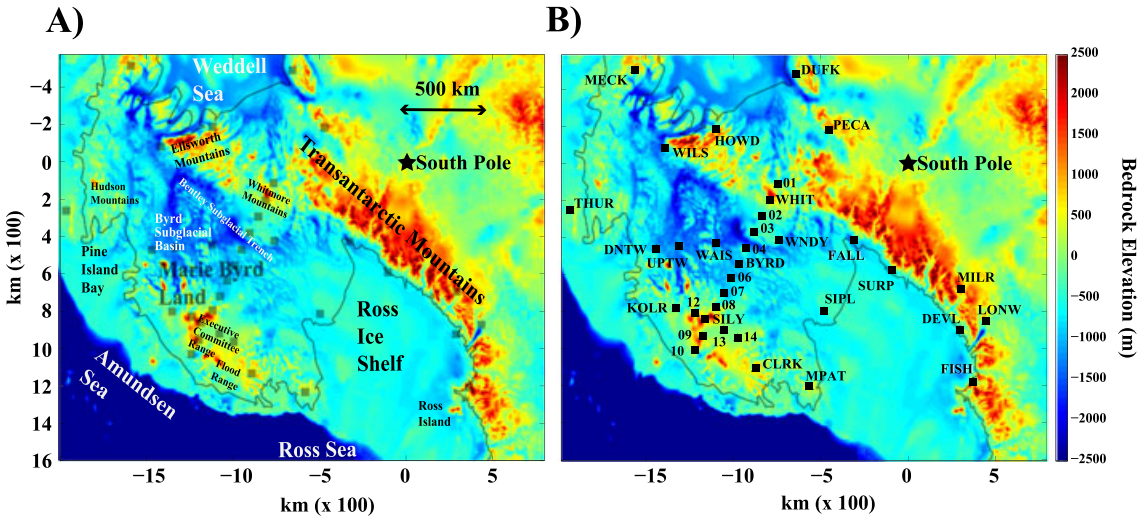

Figure 1. (a) Principal geographic features of West Antarctica, shown atop BEDMAP2 subglacial topography [*Fretwell et al.*, 2013], with the approximate Antarctic coast delineated. Grid easting and northing coordinates are kilometers relative to South Pole. (b) POLENET-ANET station locations through 2012. Fishtail Point (FISH) and Lonewolf Nunatak (LONW), as noted in the abstract, are located on either side of the Transantarctic Mountains. Other station name/location associations can be found in Table 1.

continental surface), with subglacial surface elevations as low as 2500 m below sea level. This contrasts notably with the East African and Basin and Range provinces, where buoyant warm mantle uplift results in mean elevations that are 1–2 km higher. With the exception of the relatively cool Baikal rift [*Liu and Gao*, 2006; *Tiberi et al.*, 2003; *ten Brink and Taylor*, 2002; *Cooper et al.*, 1987, 1995], continental rift provinces do not reside at such low elevations except at margins characterized by much greater crustal thinning and/or proximity to recently emerged oceanic spreading centers and oceanic crust (e.g., Gulf of California or Afar; *McClusky et al.* [2010]). The highest elevations (above approximately 2500 m) are restricted to the boundaries of the rift system, Transantarctic Mountains (TAM), Ellsworth Mountains, Whitmore Mountains, and the Marie Byrd Land (MBL) dome, including the Holocene volcanically active Executive Committee and Flood Ranges and outlying volcanoes to the east. These trachytic shield volcanoes sit atop occupy an uplifted and faulted basement of alkaline basaltic rocks and have erupted basaltic lavas similar to oceanic island basalts sampled in known mantle plume systems [*LeMasurier and Rex*, 1989; *LeMasurier*, 2008]. Multiple studies indicate that elements of this magmatic and volcanic system are presently and/or have been very recently active [e.g., *Blankenship et al.*, 1992; *Lough et al.*, 2013]. Although the nonglacial seismicity of the continental interior is remarkably low, it is detectable with regional seismographs, and recent improvements in monitoring have identified events interpreted as both due to faulting [*Winberry and Anandakrishnan*, 2003] and magmatism [*Lough et al.*, 2013]. Unraveling the tectonic structure and history of the WARS is complicated due to the vast West Antarctic Ice Sheet (WAIS) that covers much of the region, obscuring direct access to underlying bedrock. The general stability of the WAIS and linkages between the evolution of the ice sheet and underlying rift system and adjacent Transantarctic mountains have long been recognized as being of fundamental importance to understanding Antarctic Ice Sheet evolution [e.g., *Wilch et al.*, 1993; *Wilch and McIntosh*, 2000; *Pollard and DeConto*, 2009].

1.2. Seismic Constraints on Crustal Thickness in West Antarctica

[3] Much of our understanding of the WARS and its tectonic relationship to surrounding regions is derived from seismological data. The Transantarctic Mountains (TAM) constitute one of Earth's most significant intracontinental tectonic transitions, broadly delineating the boundary between fast upper mantle and thick crust within the East Antarctic Craton (EAC) and the slower upper mantle and thin crust of the West Antarctic Rift System (WARS) [*Sieminski et al.*, 2003; *Danesi and Morelli*, 2001; *Ritzwoller et al.*, 2001; *Morelli and Danesi*, 2004; *Wiens et al.*, 2012]. In association with gravity studies of the TAM, prior seismic studies have revealed crustal thickness of as low as 20±2 km for parts of the WARS [*Bannister et al.*, 2000].

[4] The TAMSEIS (TransAntarctic Mountains Seismic Experiment) experiment [*Reusch et al.*, 2008; *Watson et al.*, 2006] was a pioneering network of broadband seismographs in Antarctica. TAMSEIS crossed the TAM boundary into the EAC to characterize the WARS/EAC transition in the vicinity of McMurdo Sound, revealing low lithospheric and upper mantle velocity structure beneath Ross Island and extending 50–100 km beneath the TAM. Joint receiver function, phase velocity, and gravity analysis using TAMSEIS data [*Lawrence et al.*, 2006] yielded crustal thickness estimates of ∼20 km below Ross Island to a maximum of ∼40 km below the crest of the TAM, with EAC crustal thicknesses ∼35 km. Also identified in this study was the presence of only a thin (∼5 km) buoyant crustal TAM root, indicating that topography in this region is substantially gravitationally compensated by buoyant mantle. However, while seismic studies to date have mapped out sections of the WARS crustal and upper mantle structures

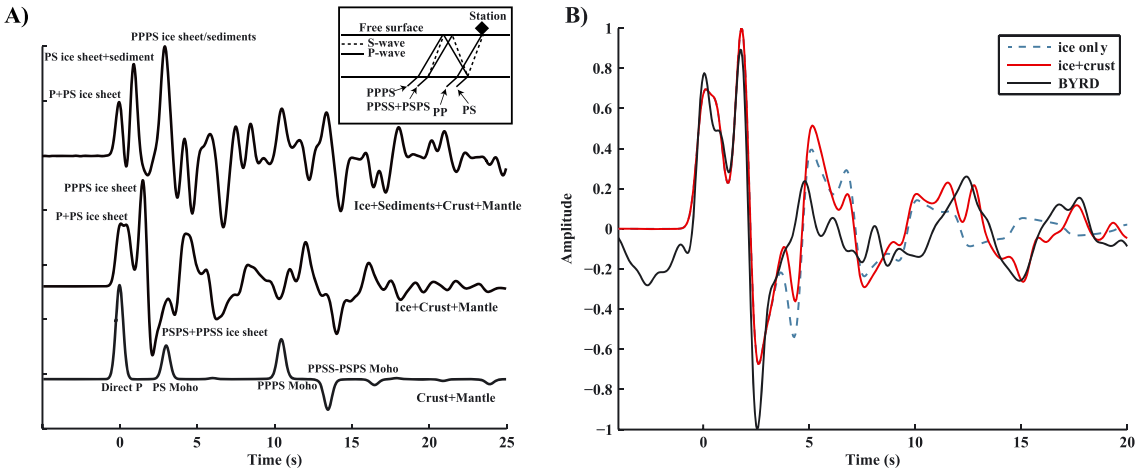

Figure 2. (a) Synthetic reflectivity forward modeled PRF waveforms showing characteristic ice sheet and sedimentary basin features. The models feature a 2.5 km thick ice sheet (Vp = 3.87 km/s; Poisson's ratio ν = 0.33), a 1 km thick sedimentary basin (Vp of 0.9 km/s; ν = 0.25), a 30 km thick crust, and an incident wave with a slowness 0.05 s/km. Because of the large seismic impedance contrast between the ice sheet and underlying crustal structure, and low ice sheet seismic attenuation, note that reverberations within the ice sheet commonly completely obscure Moho-associated phases used to determine crustal thickness. (b) Top-down fitting process for inversion priors at station BYRD. Note the great improvement brought to the fit in the later portion of the PRF by the addition of a simple crustal structure.

[*Lawrence et al.*, 2006; *Winberry and Anandakrishnan*, 2004; *Anandakrishnan and Winberry*, 2004], these studies have necessarily focused on geographically limited targets such as the TAM East-West Antarctica transition, necessitating a larger effort incorporating a more spatially extensive network of seismographs to produce continent-scale structural models that can be applied to better understand WARS tectonics and to inform WAIS modeling efforts. This motivation produced the POLENET-ANET project, funded as part of the International Polar Year (IPY), which has deployed a seismographic and geodetic network of unprecedented duration and scale across the WAIS/TAM region [e.g., *Wiens et al*., 2013].

1.3. Seismic Methodologies

1.3.1. Receiver Functions and Forward Modeling

[5] P-to-S receiver function (PRF) and S-to-P receiver function (SRF) studies provide robust methodologies for detecting seismic impedance contrasts and have been widely and successfully used to constrain crustal and mantle discontinuity structures. The advantage of this approach lies in its ability to enhance converted phases (P-to-S in the case of PRFs and S-to-P in the case of SRFs) and allows for simple interpretation in light of the zero phase output inherent to deconvolution process. The deconvolution step, where the vertical component of the seismogram is deconvolved from the radial component of the seismogram (for PRFs), is an ill-posed problem that is inherently unstable and/or noisy. Because of this, a variety of time- and frequency-domain approaches [*Park and Levin*, 2000; *Bostock*, 2004] have been applied to regularize the receiver function solution.

[6] Receiver function analysis for constraining crustal thickness has recently been performed for portions of the East Antarctic craton [*Reading*, 2006], for the TAM through TAMSEIS [*Lawrence et al.*, 2006; *Hansen et al.*, 2009], and for the Gamburtsev region AGAP projects (composed of GAMBIT (aerial geophysical survey) and GAMSEIS (seismic) with a focus on the Gamburtsev subglacial Mountains). [*Hansen et al.*, 2010]. However, receiver functions acquired over complex low-velocity shallow structures, such as ice sheets and sedimentary basins, can be very difficult to interpret via the most straightforward means (i.e., the *h-k* stacking method of *Zhou and Kanamori* [2000] and common conversion point stacking imaging) because of strong *P* wave multiples that mask P-S Moho and other key seismic phase conversions [e.g., *Wilson and Aster*, 2005]. In particular, a thick ice sheet generates strong and slowly attenuating P multiples that mask deeper P-S conversions, including conversions from the Moho that are key to estimating crustal thickness. One potential approach is to deconvolve an ice sheet response signal [*Cho*, 2011], but the complexity of the interactions between the various layers limits its robustness.

[7] Receiver function studies in West Antarctica are sparse and have previously been limited to a few small-scale or very sparse deployments, notably the pioneering ANUBIS (Antarctic Network of Broadband Seismometers) array and the Ross Sea component of the TAMSEIS array. Thick ice sheet coverage, typical for most of Antarctica, can result in the complete masking of conventionally interpreted phases in PRFs. SRFs tend to be less sensitive to these effects in theory but also have lower frequency content and present smaller data sets (due to poor signal to noise ratios on the incoming *S* waves and a more restrictive teleseismic distance range). To complicate matters further, West Antarctica hosts a number of deep subglacial troughs [*Karner et al.*, 2005; *Bell et al.*, 1998], which may contain low-velocity sediment deposits, thus further obscuring the PRF signatures. To extract meaningful information from PRFs over ice sheets, ANUBIS efforts focused on fitting PRF signatures with a simple grid searched forward model solution [*Winberry and Anandakrishnan*, 2004, 2003], thus yielding rough estimates of both crustal thickness and, in some cases, subglacial

sediment characteristics. An example of this approach, as well as the impact of ice and sediments on the PRF signature, is shown in Figure 2.

[8] For this approach to be successful, very accurate measurements of the ice thicknesses are required (for ANUBIS, these values were obtained through drilling and previous reflection surveys). The resulting crustal models may yield reasonable waveform fits, but due to their inherent simplicity, uncertainty estimates will be high. The backbone portion of the POLENET-ANET deployment is composed of stations deployed on nunataks, mountain crests, and coastal locations, and consequently, many of these stations present challenging local asymmetric subaerial or subice topography variations that can affect receiver functions. In such cases, evaluating the Moho depth and *Vp*/*Vs* ratio via multiple fitting [*Zhou and Kanamori*, 2000] from a simple crustal model typically does not yield convergent results due to multiple early peaks. It is therefore preferable to attempt to fit a more complex crustal structure to the PRFs.

1.3.2. Markov Chain Monte Carlo Inversion and Surface Wave Constraints

[9] Markov chain Monte Carlo (MCMC) algorithms [*Mosegaard and Tarantola*, 1995; *Aster et al.*, 2012, pp. 270] have recently gained traction in receiver function studies [*Bodin et al.*, 2012; *Agostinetti and Malinverno*, 2010; *Seiberlich et al.*, 2013] and many other areas of inverse geophysics problems due to their broad applicability to tractably solving Bayesian inverse problems. The MCMC approach samples the posterior distribution of the model space, thus facilitating nonparametric probabilistic model estimates. This method also offers the advantage of a linear increase in computation time with the number of parameters, and only the forward problem must be (repeatedly) solved to produce samples of the Bayesian posterior distribution. The algorithm explores the model space in a directed random walk fashion typical of Monte Carlo algorithms but with an added "acceptance criterion" at every step, which allows it to accept or reject the current model iteration based on a prechosen probability distribution. Model iterations that result in a reduction of data misfit are more likely to be sampled, but the acceptance criterion algorithm permits model steps resulting in higher misfits to be included in the sampling process, thus allowing for exploration outside of any local minimum.

[10] One of the primary difficulties with inverting waveforms generated from ice stations lies in fitting the amplitudes of the ice signature. Given the large amplitudes of these multiples, models may easily evolve toward unrealistic alternating low-/high-velocity layering. To penalize such model structure, it is possible regularize the MCMC inversion by adding a Total Variation (TV) seminorm term to the objective function [e.g., *Aster et al.*, 2012, pp. 186] to favor models with small numbers of discontinuities. Given the boundaries set by the prior models, large positive jumps are less unaffected overall, thus improving the likelihood of resolving a distinct Moho estimate. The TV regularization model seminorm is

$$\mathrm{TV}(\mathbf{m}) = \sum_{i=1}^{n-1} |m_{i+1} - m_i| = \|\mathbf{Lm}\|_1 \tag{1}$$

where **m** is the current model, **L** is the first-order roughening matrix, and the subscript 1 indicates the one norm. The objective function calculated at every forward model iteration then becomes a weighted sum of the misfit and the TV regularization seminorm

$$M_i = \|\mathbf{Gm} - \mathbf{d}\|_2^2 + \alpha \|\mathbf{Lm}\|_1 \tag{2}$$

where α is an empirically determined weighting factor that, as it increases, favors positive over negative velocity jumps at the cost of data fit.

[11] Receiver functions tend to be sensitive to velocity discontinuities at layer interfaces and not to the absolute velocities of those layers. Given that surface waves are sensitive to absolute velocities and not impedance contrasts, it has been shown [*Shen et al.*, 2012; *Liu et al.*, 2010] that the joint inversion of surface waves and receiver functions can greatly improve the accuracy of inverted model estimates. Alternatively, surface wave tomography models can be combined with discrete crustal thickness measurements to produce smoothed crustal thickness maps [*Assumpcao et al.*, 2013]. The latter option employed here has the advantage of being able to appropriately weight one model or the other based on error estimates and can be smoothed according to an arbitrary regularization coefficient to optimize data fit versus functional complexity.

[12] We present the results of iterative forward modeling as described above to obtain simple ice/sediment/crust models. We then apply these interim results as prior information for Bayesian MCMC inversions to determine crustal thickness. We show that this two-step process results in a tighter waveform fit, as well as accounting for crustal complexity where necessary. We then generate and describe a crustal thickness map of West Antarctica that combines our new determinations, previously published seismic constraints, and concurrent efforts in continent-scale ambient noise surface wave crustal thickness modeling.

2. Crustal Structure of West Antarctica From Receiver Function Methods

2.1. New Seismic Data

[13] Recent instrumentation development and general support by the Incorporated Research Institutions for Seismology (IRIS) Consortium [*Parker et al.*, 2011] has produced high-reliability stations for the Antarctic environment, and only a single station (KOLR) proved to be unusable in this study due to instrumentation problems. We used all data for the presently available POLENET-ANET data set, encompassing both its backbone (2008–2012) and temporary transect (Marie Byrd Land crossing; stations 01–14; 2010–2012) components. Figure 3 shows stations and the distribution of teleseismic earthquake sources utilized in this study. Approximately 1300 events from 30 to 90° distance were examined, with the transect stations recording approximately 50% of that number due to a shorter deployment period.

2.2. Receiver Function Computation and Forward Modeling

[14] We compute PRFs by applying a multitaper deconvolution approach [*Helffrich*, 2006; *Park and Levin*, 2000], which provides the advantage of low spectral leakage and precludes the necessity of searching over any regularization

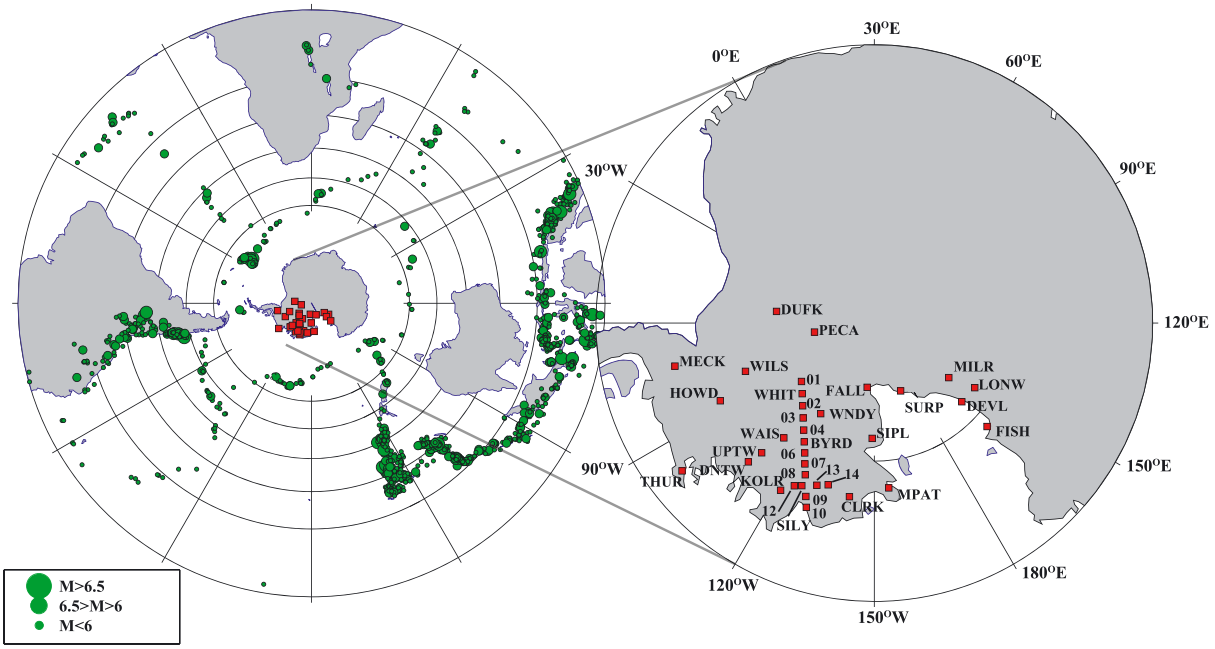

Figure 3. POLENET-ANET seismographic deployment and teleseismic source distribution (November 2008 to January 2012) used in this study. A temporary transect crossing Marie Byrd Land (01–14) was deployed for 2 years within the broader network of longer-term stations.

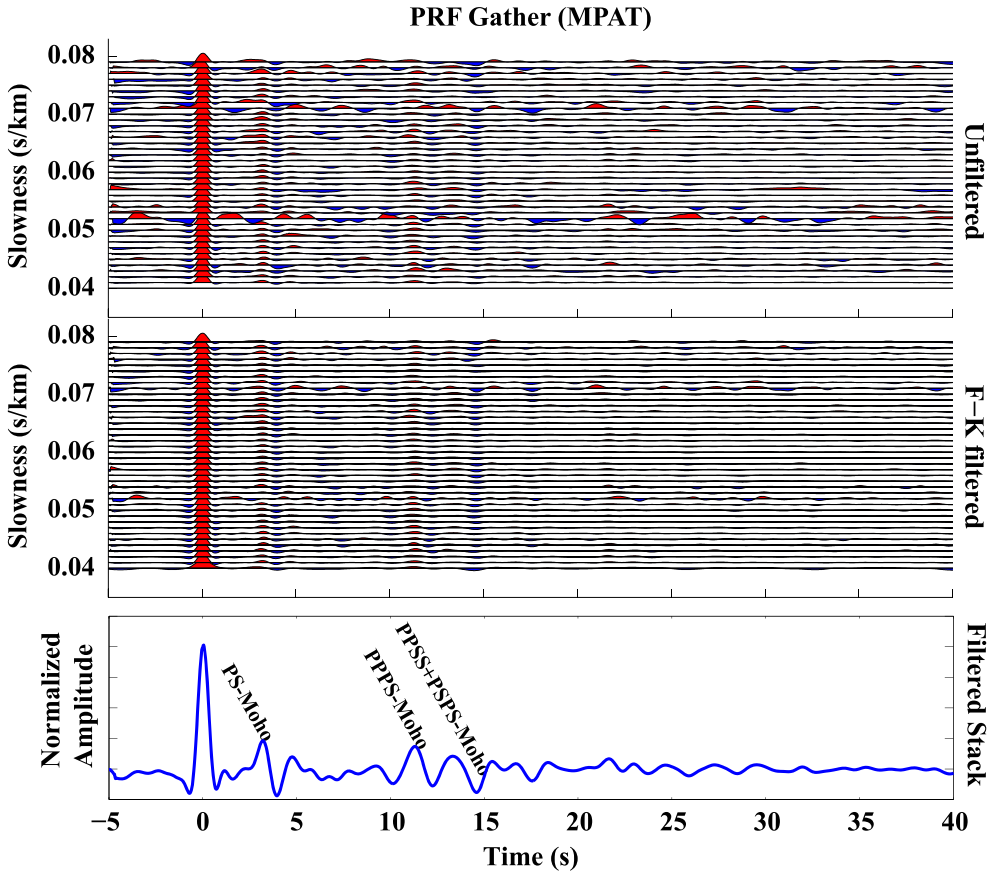

Figure 4. Representative PRF gathers from bedrock station MPAT arranged with slowness, showing the effect of *f-k* domain filtering [*Wilson and Aster*, 2005] with principal Moho/free surface-associated phases indicated. Gathers have been moveout corrected for a PPPS conversion arising from a Moho at 30 km depth.

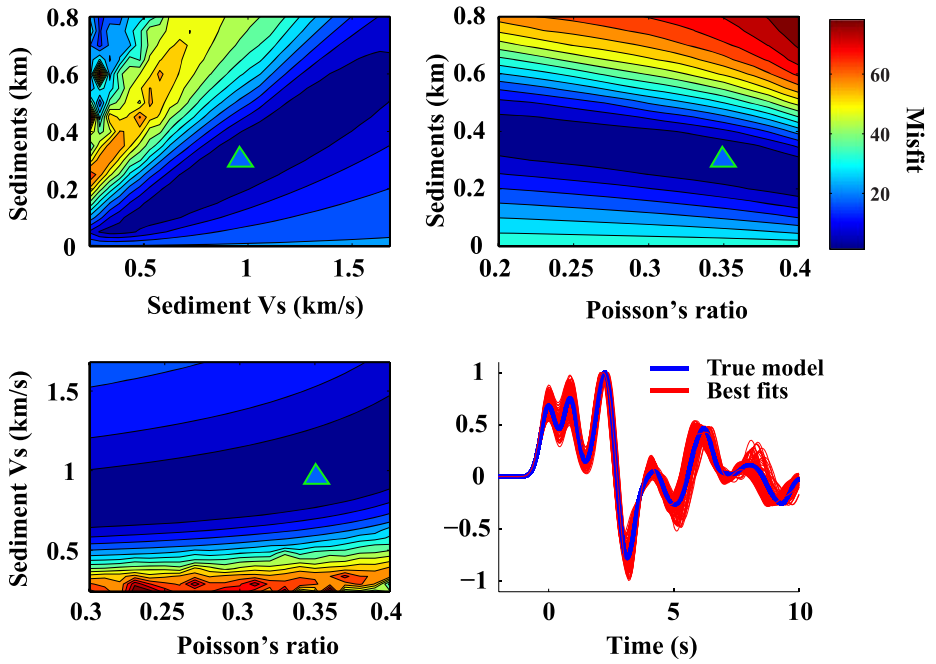

Figure 5. Synthetic exploration of the tradeoffs (two-norm PRF misfits) between various sediment parameters. The true model consists of 300 m of sediments with a Poisson's ratio of $\nu = 0.35$ and $Vp = 2$ km/s. For this thickness, the trade-off with the Poisson's ratio results in a thickness confidence interval of ~50–100 m around the true model, though this error scales with sediment thickness. The model resulting in the best fit (two norm) is indicated by the triangle in the parameter space plots, which also denotes the true model in this case. The Poisson's ratio generally has a minimal effect on fit and is this relatively weakly constrained.

parameter, and subsequently apply *f-k* domain filtering [*Wilson and Aster*, 2005] to reduce noise in the PRF gathers via suppression of nonphysical moveout velocities in the PRF gathers (Figure 4). Given that the main goal here is to constrain crustal thickness while dealing with particularly complex PRFs, we focus mainly on correctly fitting phases and less on amplitudes. As such, we compute PRF stacks based on a slowness correction for the crustal PPPS multiple, which is a valuable indicator of crustal influences on the PRFs through the ice sheet multiples in light of its larger amplitude.

[15] To recover initial crustal thickness information from receiver functions recorded on ice sheets, we forward model synthetic data using a reflectivity algorithm [*Ammon*, 1991] and use multitaper deconvolution [*Park and Levin*, 2000; *Helffrich*, 2006] to produce synthetic PRFs. Through a grid search approach, we construct from the top down a simple model, starting with the ice sheet (with valuable thickness estimates provided by BEDMAP2 [*Fretwell et al.*, 2013]) and adding possible subice sediments with varying velocities and Poisson's ratios. We choose first to synthetically explore the trade-off between the various sedimentary basin parameters for an arbitrary ice/sediment/crust model to gain a better understanding of model uncertainty. Figure 5 shows that the unknown Poisson's ratio for subglacial sediments, assuming a fixed density, results in a roughly ± 75 m uncertainty on a 300 m sedimentary basin for a Poisson's ratio range of 0.15–0.45. Nearly identical waveform fits can be reproduced by exploiting the tradeoffs between Poisson's ratio, thickness and velocity, though the effect of varying parameters

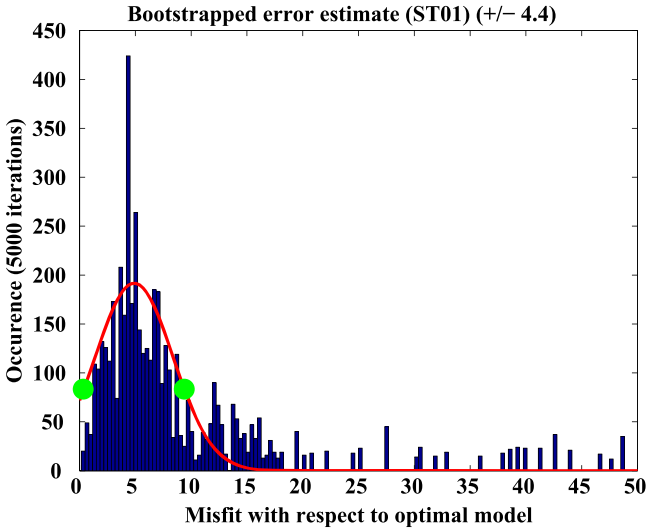

Figure 6. Example bootstrap analysis at ST01. For each station, we generate 5000 bootstrapped PRFs from the data and compute the misfit for the first 4 s with respect to the best fitting models in Figure 7. This allows us to estimate 95% confidence intervals by assuming that the bootstrapped misfit is a Gaussian normal distribution, with 95% confidence limits denoted by the green circles. For ST01, the 95% confidence interval yields a misfit range of ±4.4.

scales with sediment thickness. Ultimately, the thickness, and velocity parameters are well recovered, but a variation in the Poisson's ratio has a minimal effect for such thin layers.

[16] Figure 7a shows examples of the grid search forward modeling approach, where we searched across sediment thickness, sediment velocity, and sediment Poisson's ratio. A distribution of the models within a 95% confidence interval is also shown. Given the typically lower velocity of the sediments with respect to the ice sheet, the uncertainty from the ice sheet will result in a comparatively smaller error on the sedimentary basin thickness, with uncertainties in ice thickness propagating into the sediment estimates roughly divided by the ratio of inferred ice/sediment velocities. This error is (conservatively) summed along into a roughly 95% confidence ellipse determined via forward model grid search, and we estimate the ellipse by bootstrapping the observed station PRFs to produce a pseudo-normal distribution of misfit with respect to the best fitting synthetic solution computed from the PRF stacks shown in Figure 7. An example of this for station ST01 is displayed in Figure 6. Model fitness is ultimately determined by a least squares minimization between synthetic and observed PRFs using the first 4 s.

[17] During forward modeling, we allowed *Vp* for subice sediments to range from 0.5 to 3 km/s, while fixing the subice sheet sediment density to $\rho = 2.4$ g/cm^3 [e.g., *Studinger et al.*, 2004]. We seek the simplest physically plausible models necessary to fit the waveforms, though variations in the sediment densities are likely. Ice velocity was fixed at 3.87 km/s with $\nu = 0.33$, based on studies of *P* wave velocity in glacial ice of various temperatures [*Kohnen*, 1974]. It should be noted that the root-mean-square velocity for thinner ice sheets may vary due to the presence of low-velocity firn layers, which may add additional uncertainty to ice and sediment estimates for shallower ice sheet sites, but is not incorporated here.

[18] After an initial fit was obtained for the shallow structure, we appended a uniform crust to the model, setting crustal *Vp* to a nominal value of 6.3 km/s and fixing ν at 0.27, and evaluated the fit for the first 25 s of the computed PRF. Figure 7b shows examples of crustal-scale forward modeling fits, along with curves showing the best parameter fits. Following this final forward modeling step, we next used these rough estimates in constraining priors in a Bayesian inversion of PRFs for structure, as described below.

2.3. Additional Modeling Considerations

[19] Difficulties in modeling the delay of the P-S conversion from the base of the ice sheet relative to the later PPPS from within the ice sheet were still encountered for a few stations within the Marie Byrd Land transect (ST04, ST06, ST09, SIPL). Possible explanations include seismic anisotropy in the ice sheet [*Bentley*, 1971] or variable basal dip. Basal dip can also produce substantial timing differences between the predicted ice sheet multiples for a given thickness and the computed PRFs. Failure to correctly model the earliest portion of the PRFs could propagate into poor crustal fits during the subsequent grid search, and an inadequately modeled ice sheet may furthermore force later inversion steps to attempt to compensate for this problem by generating rough or nonphysical models (e.g., highly oscillatory models featuring large amplitude alternating low- and high-velocity zones). The Fresnel zone width for a teleseismic body wave at the base of a 3 km ice sheet is on the order of 4 to 10 km [e.g., *Lindsay*, 1989] so smaller spatial wavelength bed gradient features not necessarily visible in BEDMAP2 subice topography could explain some unusual stations. Stations deployed on nunataks also typically yielded less well constrained results attributable to extreme topography and possible steeply dipping complex shallow structure, resulting in multiple early peaks and highly oscillatory PRFs (e.g., PECA, HOWD, WILS, DUFK, MECK). This suggests that crustal to mantle-scale structural studies in Antarctica are probably generally better facilitated by ice-sited stations than by stations deployed on isolated bedrock features. Such bedrock outcrops can also feature significantly greater wind noise and attendant susceptibility to environmental damage due to their topographic prominence [*Anthony*, 2013]. Figure 8 displays examples of poorly fitted early portions of PRFs and the impact on multiples for varying degrees of basal dip. An ice sheet presenting a basal dip that decreases the apparent incidence angle of the ray with respect to the ice sheet will result in a slightly delayed PS conversion from the ice sheet and a much earlier PPPS multiple, thus potentially accounting for the mismatch in the modeled ice sheet and masquerading as a sediment layer.

[20] We can explore for consistent data features associated with simple anisotropy or basal dip by examining PRF gathers arranged by event back azimuth. Figure 9 shows azimuthally binned gathers for a few stations for which a simple ice/sediment/crust model was insufficient. For example, later multiples at ST04 show substantial azimuthal dependence, suggesting some degree of geometrical complexity to the ice sheet, though the early multiple seem relatively unaffected. We noted some cases (ST04, ST06 where solely the first P-S conversion from the base of the ice sheet is mismatched even though the general character of the later multiples can be described fairly well through a very simple ice/sediment/crust model).

[21] Although we do not implement a methodology here to model dipping layer PRFs, or better yet, finite difference modeling of the ice-rock interface, future studies utilizing PRFs over ice sheets should explore basal topography effects. We note that a small basal dip can account for much of the delay in the ice sheet PPPS and that there is a trade-off with inferred low-velocity subice (e.g., sedimentary basin) structure, although the effect on the PS phase is opposite. One must therefore be cautious when simply fitting the PPPS from the ice sheet to infer the presence of a sedimentary basin if the early waveform fit is poor, even if the ice thickness is well constrained, if there is a good deal of azimuthal variation on the timings of the early PRFs. Where the early fit is very good, however, or the later multiples can easily be matched by a simple crustal model, a sedimentary basin is more likely to be resolvable, and we can ultimately use this information to build a more robust prior for subsequent inversion, as described below.

2.4. Implementation of Markov Chain Monte Carlo Inversion

[22] In the implementation of the MCMC inversion, we assume a Poisson's ratio of 0.27 for the crust and allow the velocity of internal layers to vary freely as constrained

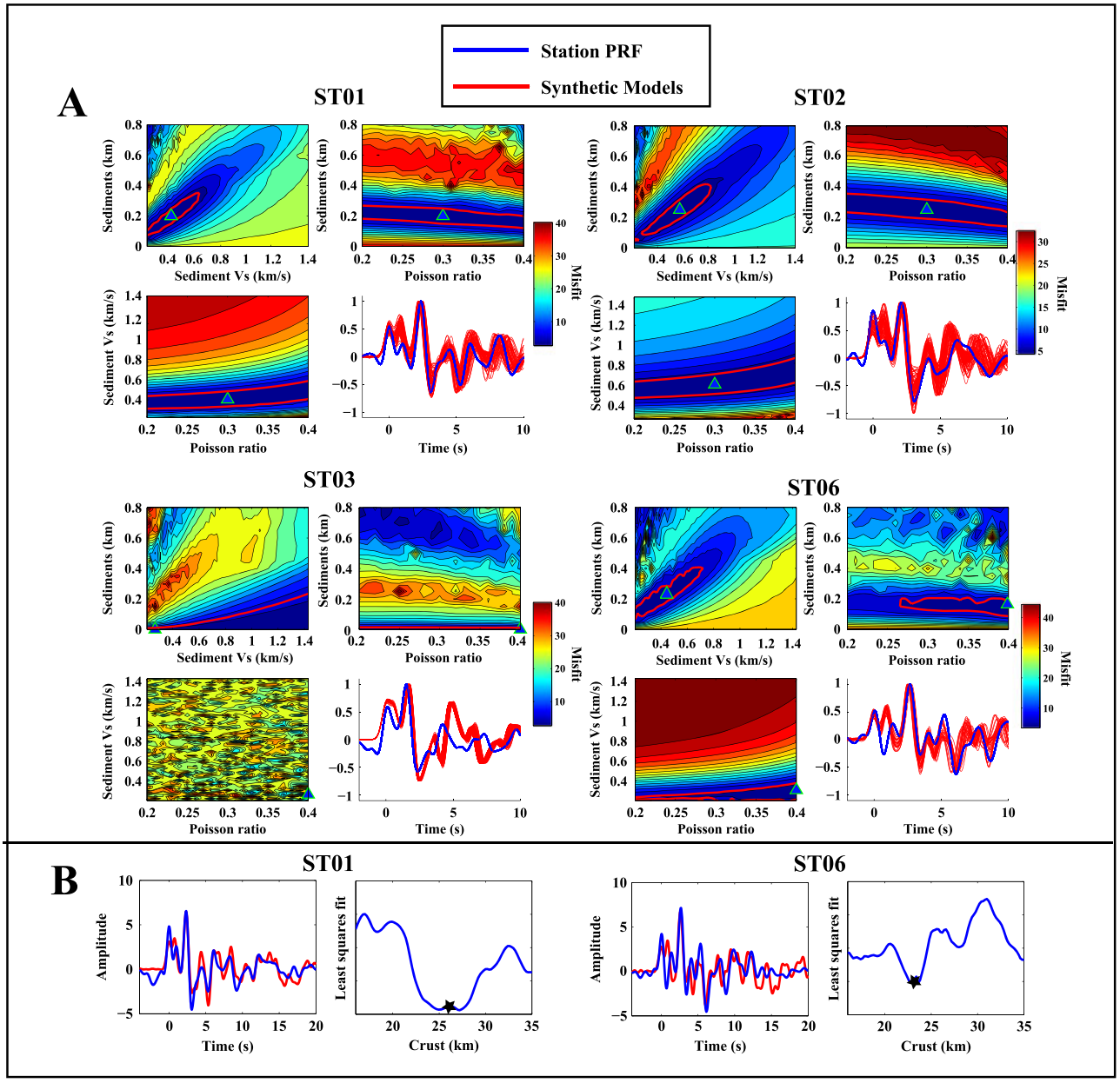

Figure 7. Examples of initial forward modeled PRFs with possible subice sediment contributions (two-norm PRF misfits). (a) First 10 s of forward modeled PRFs for stations ST01, ST02, ST03, and ST06, with the best fitting models being denoted by the green triangles. The red contours further denote the range in parameters that correspond to 95% confidence intervals as determined by Figure 6, and a sampled distribution of this model space is shown alongside the stacked station PRFs in the bottom right panels. ST03 displays no apparent contribution from sediments, while ST02 and ST06 feature slightly thicker sediment layers. The model distributions at ST06 and ST04 (not shown) also suggest high Poisson's ratios for the sediment layers, which could be representative of saturated sediments. All other stations show relatively flat Poisson's ratio distributions, as seen for ST01 and ST02, which is expected given the results of synthetic experiments (Figure 5). (b) Further fitting of a simple crustal structure for stations ST01 and ST06. Outlined black stars indicate best fit solutions. Typically, if the early portion of the PRF can be fairly accurately modeled, then the later portion can also be well fit through the simple addition of a uniform crust. These crude structures were subsequently employed to constrain priors for Bayesian inversion to arrive at final estimates of ice and crust thickness.

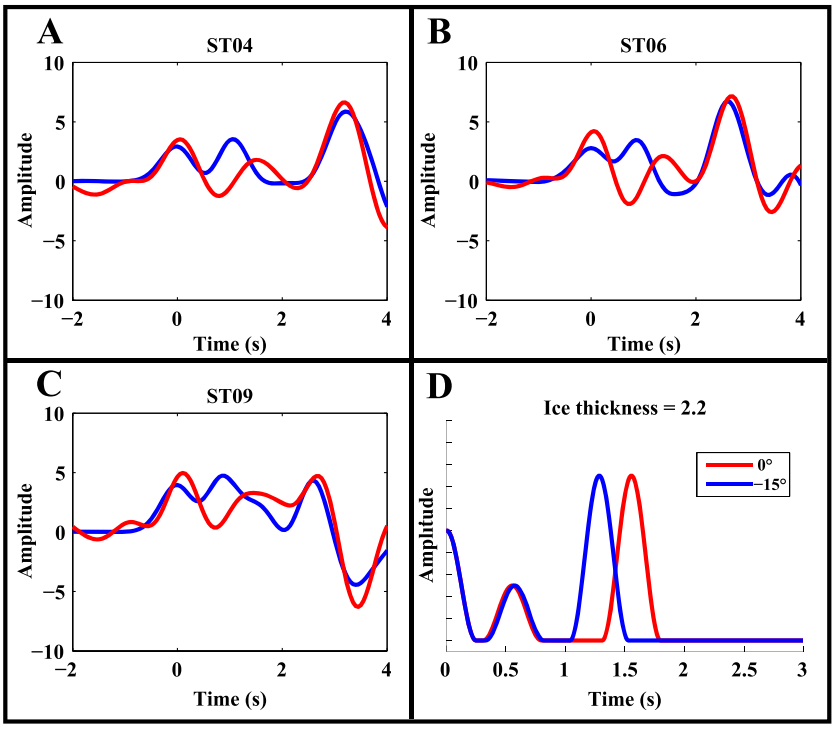

Figure 8. (a–c) Examples of poorly fit ice thicknesses for difficult stations. (d) Synthetic demonstration of the effect of a dipping ice sheet on the modeling of early multiples for an ice sheet with a 15° basal dip that reduces the apparent incidence angle of the ray at the base of the ice sheet.

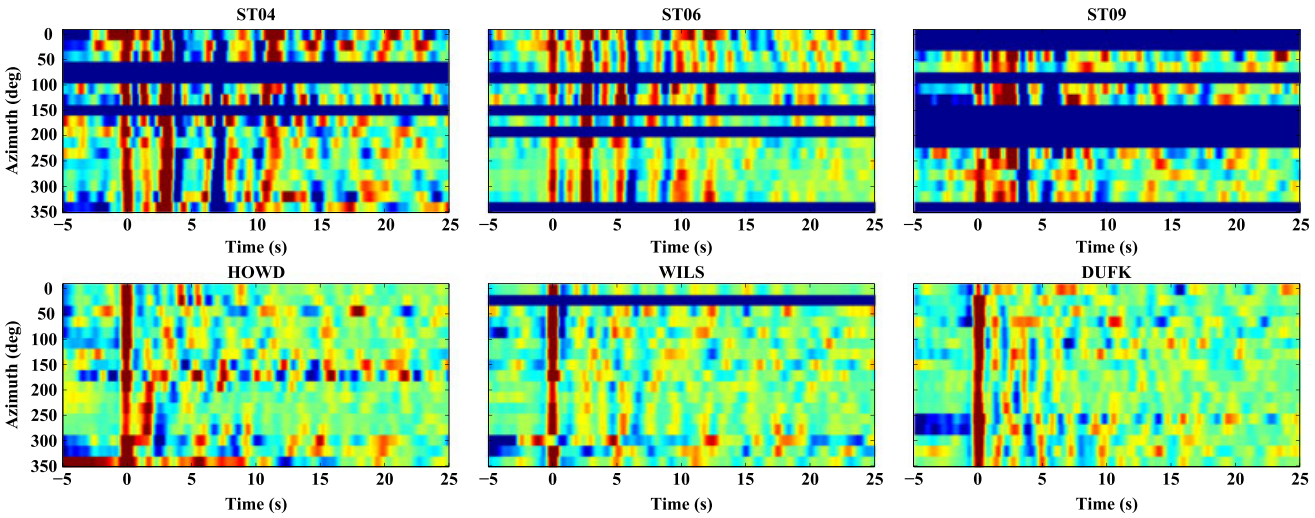

Figure 9. Azimuthally binned PRFs for stations ST04, ST06, ST09, HOWD, DUFK, and WILS, showing source azimuth variability. ST06 is unusually difficult to accurately forward model for an ice station, whereas HOWD and DUFK show a high degree of azimuthal dependance with respect to shallow structure due to their locations on the flanks of nunatak structures. These effects increase uncertainties on crustal thickness estimates. Only a small number of stations exhibited such complexities, and similar gathers for all stations are shown in the supporting information.

Table 1. Crustal Thickness (From Base of Ice Sheet for Ice Stations), Subice Sediment, and Ice Sheet Thickness Values for POLENET-ANET Stations (Figure 1), Determined by Receiver Function Analysis and MCMC Modeling[a]

Station	Lat	Lon	Elev (km)	Ice (km)	ϵ_{ice} (km)	Sed (km)	ϵ_{Sed} (km)	$V_{s,Sed}$ (km/s)	Moho (km)	ϵ_{Moho} (km)	Location
ST01	–83.2279	–98.7419	2.03	2.24	0.30	0.20	0.11	0.45	28.0	3	Ice sheet
ST02	–82.0690	–109.1243	1.72	2.14	0.09	0.27	0.12	0.61	32.1	2	Ice sheet
ST03	–81.4065	–113.1504	1.66	2.23	0.15	0	0	-	24.3	2	Ice sheet
ST04	–80.7150	–116.5782	1.52	2.96	0.09	0.35	0.12	0.62	20.8	3	Ice sheet
ST06	–79.3316	–121.8196	1.52	2.40	0.09	0.23	0.1	0.45	22.4	2	Ice sheet
ST07	–78.6387	–123.7953	1.59	2.61	0.15	0	0	-	23.6	3	Ice sheet
ST08	–77.9576	–125.5313	1.78	2.30	0.09	0.15	0.1	0.6	24.5	2	Ice sheet
ST09	–76.5309	–128.4734	2.25	2.14	0.20	0.45	0.6	0.78	29.6	2	Ice sheet
ST10	–75.8143	–129.7489	1.75	1.13	1.00	0.3	0.12	0.7	28.7	2	Ice sheet
ST12	–76.8970	–123.8160	2.20	1.92	1.00	0	0	-	22.1	2	Ice sheet
ST13	–77.5609	–130.5139	1.86	1.98	0.09	0.25	0.5	0.8	30.2	4	Ice sheet
ST14	–77.8378	–134.0802	1.64	1.73	0.09	0	0	-	27.2	2	Ice sheet
CLRK	–77.3231	–141.8485	1.04	0.00	-	0	0	-	30.0	2	Mt. Clarke
KOLR	–76.1545	–120.7276	1.89	1.79	0.30	0.62	0.62	0.61	-	-	Kohler Glacier
WNDY	–82.3695	–119.4129	0.94	1.67	0.20	0	0	-	21.5	4	Windy
FALL	–85.3066	–143.6284	0.29	0.00	-	0	0	-	24.0	4	Fallone Nunatak
SILY	–77.1332	–125.9660	2.09	0.00	-	0	0	-	32.8	2	Mt. Sidley
DNTW	–76.4571	–107.7804	1.04	2.11	0.09	0	0	-	23.1	2	Down Thwaits
WHIT	–82.6823	–104.3867	1.29	0.00	-	0	0	-	31.5	3	Mt. Whitmore
MPAT	–78.0297	–155.0220	0.54	0.00	-	0	0	-	27.5	1	Mt. Patterson
SIPL	–81.6405	–148.9555	0.65	1.03	0.15	0.20	0.2	0.42	27.0	10	Ice sheet (Siple Dome)
MECK	–75.2807	–72.1849	1.08	0.00	-	0	0	-	26.5	4	Merrick Mountains
HOWD	–77.5285	–86.7694	1.50	0.00	-	0	0	-	37.0	4	Howard Nunatak
WILS	–80.0396	–80.5587	0.69	0.00	-	0	0	-	30.0	5	Wilson Nunatak
DUFK	–82.8619	–53.2007	0.97	0.00	-	0	0	-	38.4	5	Dufek Massif
PECA	–85.6124	–68.5527	1.51	0.00	-	0	0	-	37.0	5	Pecora Escarpment
LONW	–81.3466	152.7350	1.55	0.00	-	0	0	-	45.0	5	Lonewolf Nunataks
MILR	–83.3063	156.2517	1.90	0.00	-	0	0	-	45.0	10	Miller Range
SURP	–84.7199	–171.2018	0.41	0.00	-	0	0	-	26.5	2	Cape Surprise
DEVL	–81.4757	161.9745	0.10	0.00	-	0	0	-	18.0	4	Devlin Island
FISH	–78.9276	162.5652	0.27	0.00	-	0	0	-	17.0	4	Fishtail Point
WAIS	–79.4181	–111.7776	1.80	3.37	0.15	0	0	-	22.2	2	Ice sheet (WAIS Divide)
BYRD	–80.0168	–119.4730	1.52	2.45	0.09	0	0	-	24.3	2	Ice sheet (BYRD Camp)
THUR	–72.5301	–97.5606	0.24	0.00	-	0	0	-	24.1	3	Thurston Island
UPTW	–77.5797	–109.0396	1.33	2.39	0.09	0.3	0.06	0.52	20.0	10	Up Thwaits

[a]Ice thicknesses are from BEDMAP2 [*Fretwell et al.*, 2013]. Error estimates are 95% confidence intervals. Station CLRK is installed on negligibly thin ice.

by station-specific priors evaluated from initial fitting as described above. For ice sheet-deployed stations, we fix the elastic parameters of the first (ice) layer to the forward modeled prior, as we found that unrealistic models for the ice sheet may still arise in the MCMC procedure because of the strong trade-off between thickness and velocity in generating the ice sheet PRF signature. The mantle *P* wave velocity in the MCMC inversions was fixed at a nominal 8.04 km/s. Somewhat lower uppermost mantle velocities (7.7–7.8 km/s) have been recently indicated by tomography models [*Lloyd et al.*, 2013]. However, fixing the mantle velocity across this range results in nearly identical inferred structures in tests because the depth of the Moho is much more robustly constrained in receiver function modeling than the transmission/reflection coefficient. Where there is clear model convergence in the forward modeled priors (see Table 1), we also introduce sediment thickness, and the model is allowed to vary out of these values during the MCMC process. We then fit a ten-layer model with prior layer depths determined by the initial forward model step, while allowing the depths to vary freely and the velocities of the layers to vary within ±1 km/s of the crustal prior, based on the range of IASPEI91 [*Kennett*, 1991] crustal velocities. For ice sheet stations, we use an empirically determined (from examining various trade-off curves) TV regularization factor α of 0.25, while for rock stations, which do not suffer the potentially destabilizing influences of ice sheet multiples, we use a much lower degree of regularization (α = 0.02). To sample the posterior distribution in the MCMC process, we used a proposal function that allowed for the velocity and layer thicknesses to take steps of up to 1 km/s and 1 km, respectively, using realizations of a uniform random variable. This resulted in an acceptance rate of 0.3–0.5 for newly proposed models, which is within the generally optimal range for MCMC methods.

[23] Figure 10 shows example inversion results for representative rock and ice stations. Inversions for ice stations with structures that are well fit during the forward modeling steps do not vary substantially from their priors, as expected. We conservatively parameterize the crustal thickness uncertainty as the depth range over which the crustal probability begins to decay from its pre-Moho maximum to where the post-Moho peak reaches a local maximum in mantle velocities. The most likely crustal thickness determinations (the maximum a posteriori models) for all stations and associated posteriori-derived uncertainties are noted in Table 1. For a small number of stations that present particularly complex crustal structures and/or possible near-station subice

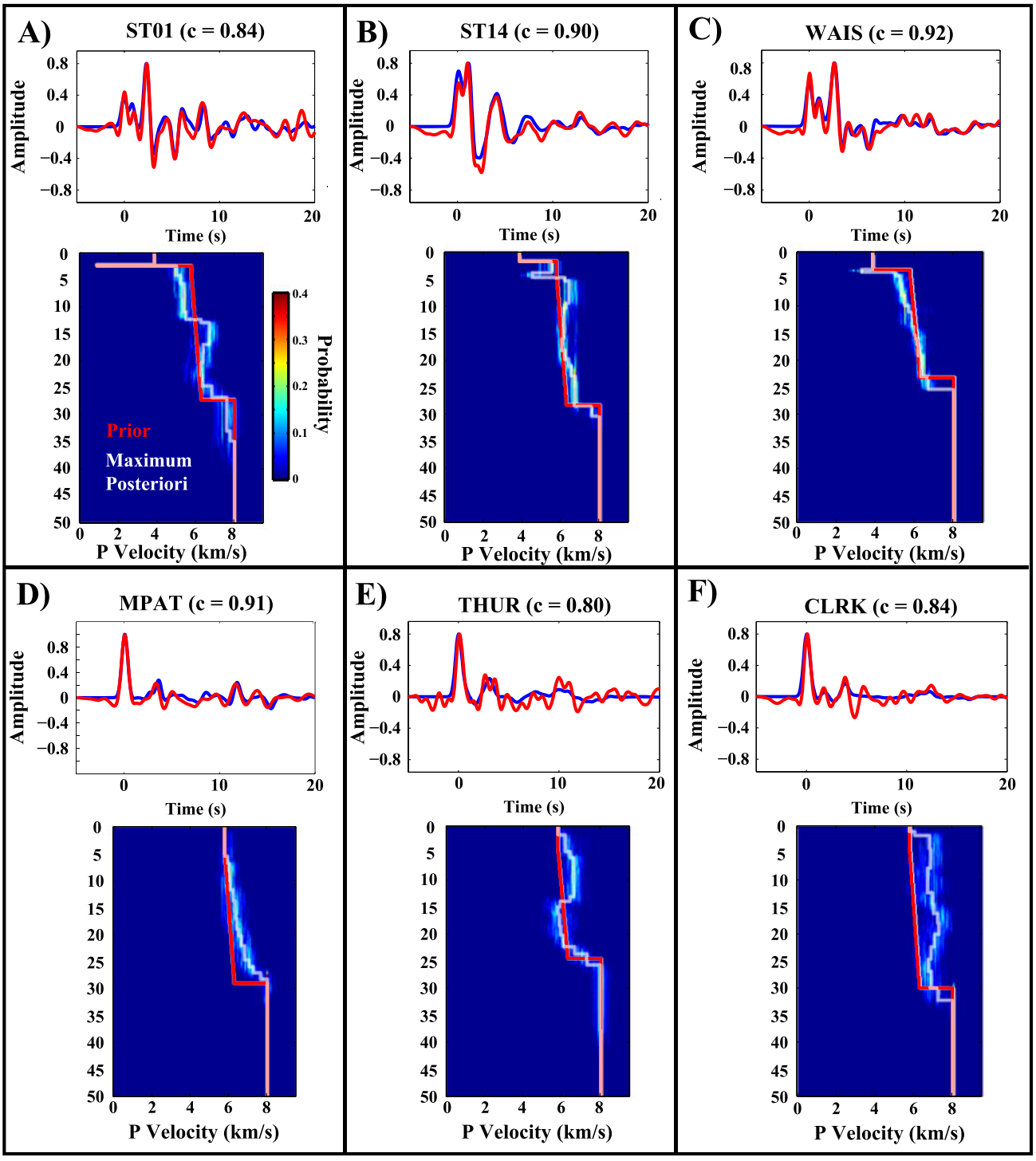

Figure 10. Representative MCMC inversion results. (a–e) Examples of probability density plots after a burn-in of 5000 model steps. Figures 10a–10c are ice sheet stations; Figures 10d–10f are rock stations. Where possible, we aim to fit a simple model (10 layers, 1 km/s maximal deviation from IASPEI91 velocities, no limit on layer thicknesses) and penalize large negative velocity jumps in the resulting model using TV regularization. Zero depth is defined at the free surface. Similar fit and model figures for all stations are displayed in this format in the supporting information.

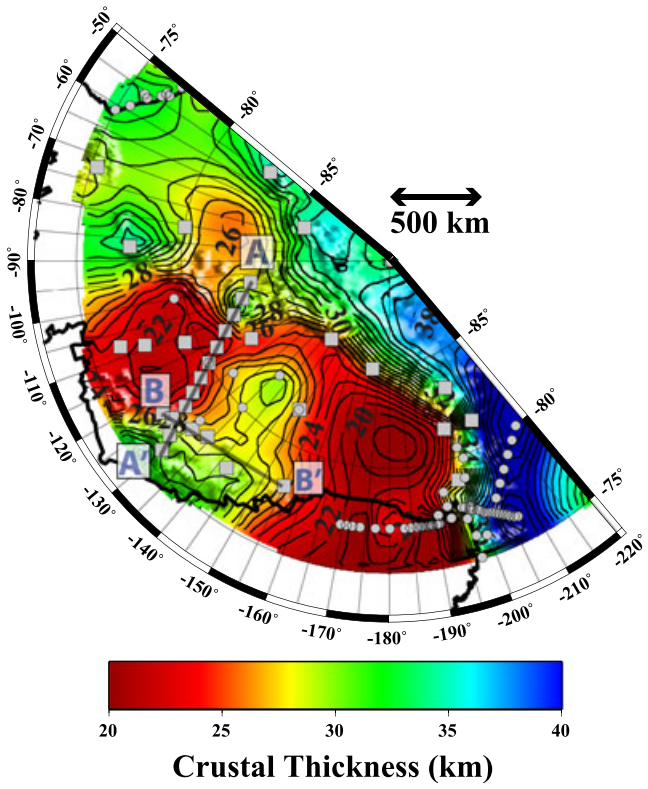

Figure 11. Crustal thickness map (from base of ice sheet to Moho) estimated for West Antarctica using POLENET-ANET (Table 1) and other seismic station constraints (supporting information), and using the continent-scale surface wave constrained estimates of *Sun et al.* [2013] as described in the text. Seismographic stations are shown as boxes; other stations are shown as smaller circles. A – A′ and B – B′ transects indicated refer to Figure 12.

topography, it was not possible to determine crustal thickness, although the only ice station presenting difficulties in this analysis was SIPL, which was treated as a special case constrained by the known (drilling-measured) ice sheet thickness. This still resulted in a highly uncertain SIPL crustal thickness estimate (27.0 ± 10 km), however. This thickness is in agreement with that (27 km) estimated by *Winberry and Anandakrishnan* [2004] for their nearby SDM (Siple Dome) station, though the error in both cases is large. As in initial model fitting, difficulties generally arose for the small percentage of stations that showed significant azimuth PRF dependencies (Figure 9), probably largely arising from subice and/or sedimentary contact dip, as well as flank structure or geometry associated with nunataks.

2.5. POLENET-ANET Receiver Function Crustal Thickness Determinations

[24] Table 1 presents comprehensive results from the forward modeled and inverted PRF receiver functions. Figure 12 shows receiver function values in seismic transect-constrained cross-section views of the lines denoted A – A′ and B – B′ in Figure 11.

[25] Crustal thicknesses across the center of the West Antarctic transect range from 21 to 28 km, with modest thickening into the MBL volcanic province up to 32.8 km, greater thickening under the Whitmore block (WHIT (31.5 ± 3 km)), and much greater thickening into the Ellsworth Mountains (HOWD (37 ± 5 km), WILS (30 ± 5 km)), though these determinations have a high degree of associated error. Stations throughout the transect present a variety of subglacial sediment thickness estimates, with the central portion of the transect, notably in the region of ST04 and ST06, displaying results suggesting several hundreds of meters of very low velocity material. This is not surprising given the pronounced subglacial topography underlying those stations and previous studies of sedimentary basins in the area. Furthermore, stations located over basin shoulders seem to lack underlying low-velocity sediments.

[26] Stations ST04 and ST06 also feature relatively thin crustal measurements (20.8 ± 3 km; 22.4 ± 2 km, respectively) that correlate with their location above very deep basins along the transect. Prior magnetotelluric study of the Byrd subglacial basin region [*Wannamaker et al.*, 1996] suggests that these features are currently inactive, consistent with a lack of seismicity associated with these structures. These constraints also confirm very thin crust on the rift side of the TAM (DEVL (18 ± 4 km); FISH (17 ± 4 km)), in the Ross Island region. It should be noted that the Moho errors reported here are strictly the output of the various

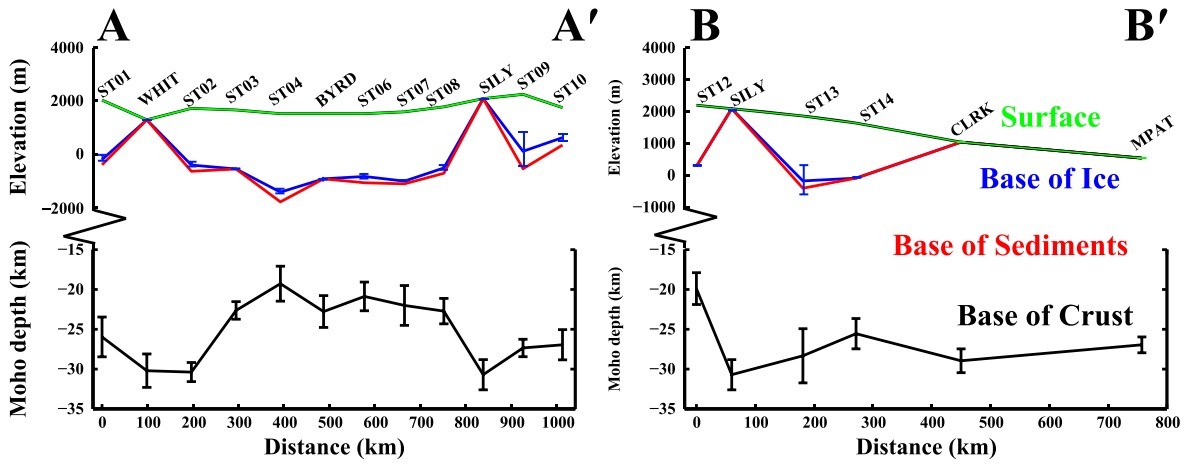

Figure 12. Linearly interpolated transect profiles (Figure 11) showing ice surface, ice base, and Moho depths. MCMC-estimated 95% confidence limits are from Table 1.

sources mentioned and are likely an underestimate of the true error. This is due to several sources of error that are difficult to quantify, such as crustal *Vp*/*Vs* ratios and the TV regularization criterion, which further restricts the model space exploration and results in tighter than expected posterior distributions. This is, however, necessary due to the evident problems associated with fitting ice sheet multiples via unreasonable models.

3. West Antarctic Crustal Thickness Constrained by Receiver Functions and Ambient Noise Surface Wave Tomography

[27] We combined our station constraints with prior estimates into a West Antarctica crustal thickness map by applying the highly smoothed but continent-scale ambient noise surface wave tomography model of *Sun et al.* [2013] as an informed interpolant. The ambient model is highly complementary to receiver function methods in that it produces a very smooth crustal thickness estimate for areas that are unsampled by the receiver function methodology but has generally lesser localized crustal thickness resolution. This modeling incorporated results from this study and from other seismic networks and experiments (e.g., AGAP, TAMSEIS, ANUBIS, and the GT and GSN networks; Tables 1 and S1 of the supporting information list these sources) to create a crustal map of Antarctica south of 75°S with a lateral discretization of 75 km. A full continent-scale map using this methodology is planned to be the subject of further work; we report here specifically on the results for West Antarctica.

[28] The crustal thickness model for West Antarctica was calculated using a least squares, second-order Tikhonov (Laplacian) regularization (with free edges) to produce a minimized second-order integrated spatial derivative across the surface. Stations utilized are summarized in the supporting information Tables S1 and S2. We solved for crustal thickness for 1550 seventy-five square kilometer areal patches covering Antarctica south of 75°S. A total of 208 seismically determined crustal thickness measurement using receiver functions were implemented. Standard deviations from Table 1 and Figure S5 were applied to weight all the constraint equations in the regularized least squares problem (A1), with the relatively sparse receiver function point constraints being weighed a factor of five greater than the much denser but less localized surface wave constraints. Crustal and ice thickness determinations for POLENET-ANET station sites can be found in Table 1, and results utilized from prior, non-POLENET, studies and stations are noted in the supporting information. The surface fit is designed to obtain an optimal smooth surface with varying curvature that optimally fits all data in the least squares sense without tectonic or other assumptions. The resolution of this model is highly nonuniform due to the highly uneven spacing of seismic stations. Spectral analysis of the surface shows that 100–150 km wavelength information is present in regions of the model where constraints are dense, such as the vicinity of McMurdo Sound. Conversely, where station coverage is exceptionally sparse, such as the southern Ross Sea, only features with spatial wavelengths of greater than approximately 400 km are resolved. The fitting methodology is described in detail in the Appendix.

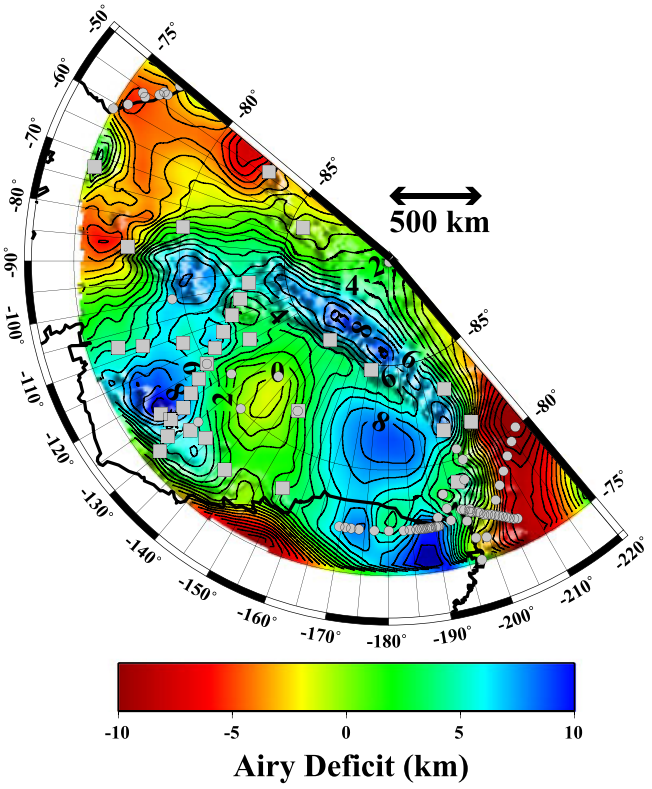

Figure 13. Crustal deficit relative to an Airy crustal topographic compensation model, calculated using rebounded topography low-pass filtered to spatial wavelengths greater than 200 km (Figure 14).

4. Topographic Support

[29] Using reasonable crustal and mantle density values, for topography to be in Airy isostatic equilibrium with full crustal compensation, each kilometer of surface topography must be supported by ∼5.5 km crustal root [e.g., *Lachenbruch and Morgan*, 1990]. West Antarctic surface elevation varies by over 3.5 km. If this topography was supported by crustal roots, we would thus predict approximately 20 km of topography on the Moho. In contrast, the Moho across the west Antarctic transect is relatively flat, with the exception of the Ellsworth Mountains, indicating that long-wavelength elevation in this region is significantly supported by the mantle. We calculate the expected, isostatic, crustal thickness using the deiced elevations, nominal values of crustal density of 2750 kg/m^3 and a mantle density of 3250 kg/m^3, and assume that crust with a surface elevation at sea level has a crustal thickness of 30 km in general agreement with global values. We then determine the thickness of crustal root that is "missing" relative to a full crustal compensation situation by subtracting the seismically determined crustal thickness from the calculated, Airy isostasy, crustal thickness (Figure 13). To eliminate effects due to crustal flexural support, we filter these results with a low-pass median spatial filter with a corner wave number of 1/200 km^{-1} (Figure 14) that is reasonable for intraplate continental topography in tectonically active regions under average to thin crustal thickness [e.g., *Hansen et al.*, 2013].

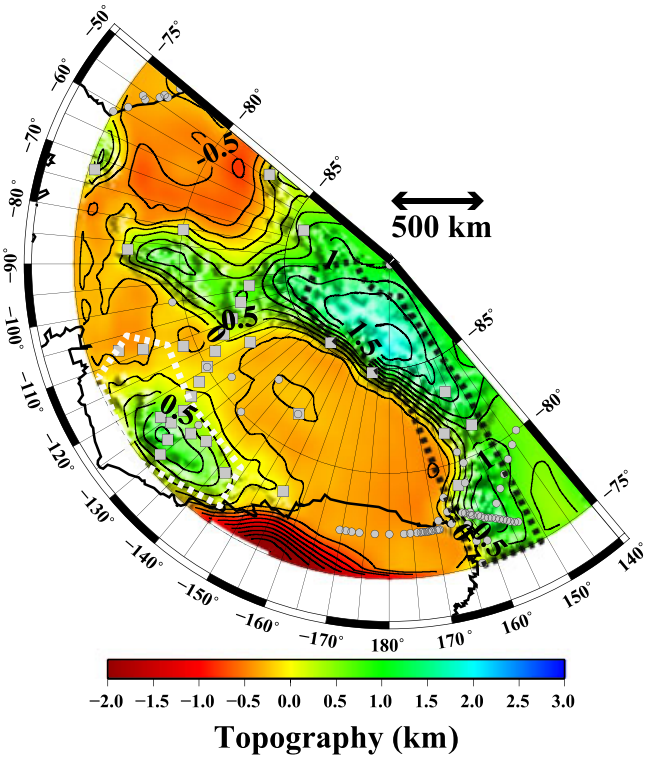

Figure 14. Ice rebound-adjusted topography, low-pass median filtered at a spatial wavelength of 200 km used in the construction of Figure 13. Dashed white and black polygons isolating the MBL dome and TAM regions, respectively, are referred to in Figure 15.

5. Discussion

[30] The results presented here provide a detailed look at the WARS region that complements the somewhat lower-resolution continent-wide recent estimates of *Baranov* [2010]. The general character of crustal thickness for the WARS (Figure 11) can be characterized as two large areas of thin (< 25 km) crust, below the Ross Sea and MBL basins, separated by a distinctly thicker ridge that extends south of the MBL dome and nearly transects the rift in the vicinity of ANUBIS station STC [*Winberry and Anandakrishnan*, 2004]. These areas of thinned crust are separated by a N-S trans-WARS ridge of thicker crust (up to 30 km) near 140°W longitude that is contiguous with the region of thicker (up to 33 km) crust beneath the MBL dome. The general uniformity of observed thin crust suggests that much of the WARS ultimately accommodated extension fairly uniformly during late Mesozoic through Cenozoic periods of extension overall. Profile results from the transect stations (Figure 12) additionally demonstrate localized crustal thinning (to < 25 km) that correlates with deep subglacial troughs. This is suggestive that these deep troughs formed during periods of focused ductile lithospheric/crustal extension, perhaps concentrated by preexisting lithospheric weak zones [*Winberry and Anandakrishnan*, 2004]. These results corroborate recent aerogravity studies that have suggested a zone of pronounced thinning in the Pine Island Glacier area (emphasized here by station DNTW (23.1 ± 1.8 km)) suggestive of localized Pine Island crustal thinning [*Jordan et al.*, 2010]. This view of migrating extensional focusing is additionally supported by evidence for episodic rift shoulder uplift in the TAM and concentrated rifting and strong localized crustal thinning at the Terror Rift near Ross Island [e.g., *Behrendt and Cooper*, 1991] that suggest that this process continues at the westernmost edge of the WARS.

[31] We note distinctly thicker crust beneath the highlands of the TAM, MBL dome, Whitmore Mountains, and Ellsworth Mountains that bound the deep basins of WARS interior. This, corroborated with higher uppermost mantle velocities beneath the Whitmore region [*Lloyd et al.*, 2013], suggests that the Whitmore Mountains constitute a distinct tectonic subprovince. Satellite gravity studies [*Block et al.*, 2009; *Bell et al.*, 1998] have also detected significant negative Bouguer anomalies under these regions that were interpreted as a substantial crustal root beneath these elevated terrains. However, across each of these regions, while thicker than the WARS interior, we observed thinner crust than required to explain the present observed elevations. Basic isostatic compensation calculations (Figures 13 and 15) indicate localized mantle support (e.g., "missing crust") for this topography, consistent with mass deficiencies indicated by gravity observations. The high elevations of Marie Byrd Land, the Whitmore/Ellsworth block, and the Transantarctic Mountains have especially notably deficient Airy-model crustal roots (Figure 15). Crustal values for the MBL region confirm sparse previous [*Winberry and Anandakrishnan*, 2004; *Block et al.*, 2009] studies suggesting widespread thin crust under the WAIS and further corroborate the presence of thin, mantle-compensated crust in the MBL dome and volcanic province. The relatively thin MBL crust (Figures 11 and 15) therefore contradicts views of a much thicker crust-compensated MBL [*Luyendyk et al.*, 2003; *Block et al.*, 2009] and reinforces the idea of warm and buoyant mantle beneath MBL [*Winberry and Anandakrishnan*, 2004].

[32] These results across the lower elevation portions of the WARS suggest that the thicker crust region extending south of the MBL dome is in a state of near crustal Airy compensation [*Jordan et al.*, 2010] but that the thinnest regions beneath the Ross Ice Shelf and the Bentley Subglacial Trough have thinner crust (by up to 6 to 8 km) than predicted by the Airy model. Although the higher elevations of West Antarctica analyzed here exhibit a crustal root deficit relative to a simply Airy compensation model, they do generally show a weak positive correlation of crustal thickness with elevation (Figure 15), as opposed to, for example, the intraplate Colorado Rockies, which display an anticorrelation of crustal thickness with elevation [e.g., *Hansen et al.*, 2013].

[33] Given the direct impact of underlying low-velocity sediments on ice sheet stability and flow pertaining to ice streaming, we present a view of thin subice sediment thickness across two transects of West Antarctica. BEDMAP2 uncertainties on ice sheet thickness are generally low throughout West Antarctica (50–150 m) with the exception of parts of MBL, where coverage is much poorer. Sediment characteristics for other stations can be found in Table 1. We notice that for stations with relatively small ice thickness uncertainties from BEDMAP2 (which is the case for much of the WAIS), the thickness of the sediments

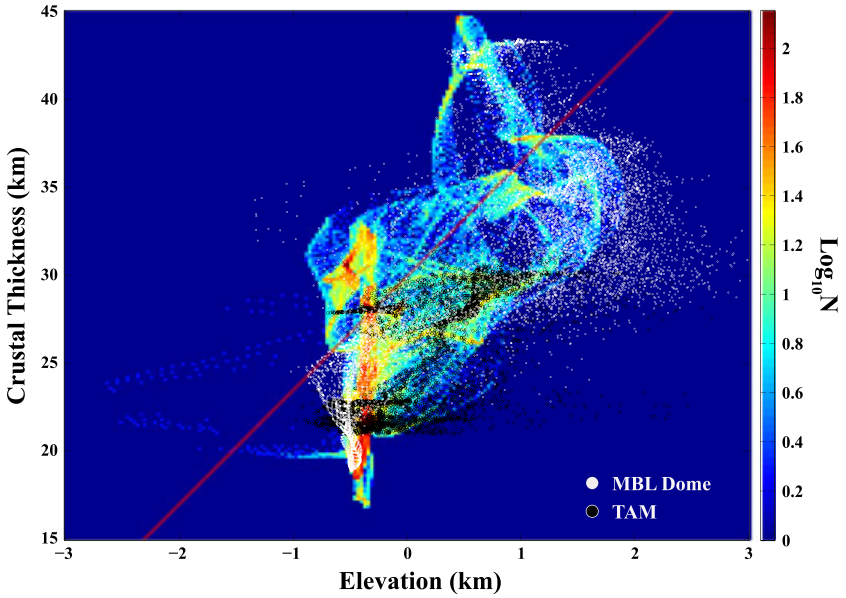

Figure 15. Histogram ($\log_{10}$) of crustal thickness (Figure 11) versus unfiltered rebound-adjusted topography (Figure 14) evaluated along 75 by 75 km cells across West Antarctica (Antarctica between 140° and 310°E longitude. The red line is a crustal Airy prediction for 30 km thick sea level elevation crust and assuming crustal and mantle densities of 2750 kg/m^3 and 3250 kg/m^3, respectively. The widely crustally undercompensated (to the right of the red line) Marie Byrd Land dome (white) and Transantarctic Mountains (black) model points are indicated atop the histogram (the geographic patches corresponding to these points are shown in Figure 14).

increases within the subglacial troughs (ST04, ST06) and falls to zero at trough shoulders. For stations in MBL, which may have BEDMAP2 uncertainties up to 1 km, large inferred sedimentary thickness uncertainties simply reflect poorly known ice thickness, which has an appreciable tradeoff with sedimentary structure during the forward modeling process. It is also notable that the Poisson's ratios for the thicker shallow sediments under stations ST04 and ST06, which sit above deep subglacial troughs, are particularly high, suggesting water saturation. Future studies involving PRFs over ice sheets could approach interpretation through a more complex forward model capable of handling dipping layers, which probably explain modeling difficulties encountered at a few stations in this study.

[34] This study further emphasizes the dramatic differences between the crust of West and East Antarctica. West Antarctica and the adjacent TAM is undercompensated by the crust over significant high-elevation provinces. East Antarctica, in contrast, has relatively overthickened crust across much of its extent [e.g., *Hansen et al.*, 2009]. This contrast between active tectonic provinces featuring relatively "rootless" mountain ranges and cratonic provinces with appreciable roots has been widely noted on other continents. Elevations of the WARS are considerably lower than those in other continental rift provinces and pose a challenging puzzle in light of robust indications of high heat flow and low velocity, low viscosity, and warm mantle. The mid-WARS ridge of thicker crust south of the MBL Dome indicates that crustal thinning is highly nonuniformly distributed along the axis of the rifting system, with thinnest crust strongly segregated to the west and east.

6. Conclusions

[35] We have demonstrated that significant difficulties involved in interpreting P-receiver functions over complex shallow media involving ice sheets can be overcome through a combination of forward modeling and inversion, even in situations where there is a limited amount of a priori information concerning ice sheet properties and solid Earth layer thicknesses and velocities. Given the extremely large impedance contrast between the crust and the ice sheet, it is imperative to correctly model the ice sheet multiples to subsequently fit a crustal model. We applied an MCMC inversion approach to PRFs from POLENET-ANET and combined these results with previous receiver function studies and ambient noise surface wave tomography to generate an updated crustal map of West Antarctica, showing details of the general thin crust underlying the West Antarctic Ice Sheet and crustal thickening into the Ellsworth and Whitmore Mountains and Marie Byrd Land dome. These measurements, combined with current tomographic efforts, support a thin crust under the WAIS overlying a slow mantle, with localized low-density mantle under the MBL dome providing substantial topographic support. We also note the confirmed presence of highly thinned crust near the newly identified Pine Island Rift from two stations. Crustal thicknesses in our model yield general estimates of the degree of long-wavelength crustal undercompensation for high-elevation portions of West Antarctica. This analysis suggests that as much as 20 km of crust may be "missing" from under the MBL and Transantarctic Mountains and indicates the presence of low density and possibly upwelling mantle in those areas. Further work with ambient noise, receiver

function, and other methodologies should facilitate improving the resolution of crustal thickness further across the continent as Antarctic seismic data continue to improve in quantity and quality.

Appendix A: Crustal Thickness Surface Estimation

A1. Methodology

[36] We estimated a crustal thickness surface for West Antarctica by fitting a second-order smoothed Tikhonov surface jointly to the station-specific thickness determinations measured in this paper (Table 1) and in previous studies (see supporting information). This procedure produces a map that reverts to the *Sun et al.* [2013] model where receiver function data were not available while allowing for smooth perturbations to incorporate regions of good receiver function sampling. The associated minimization problem can be expressed as

$$\min\|\mathbf{Gm}-\mathbf{d}\|_2^2+\alpha^2\|\mathbf{Lm}\|_2^2 \quad \text{(A1)}$$

where **G** is a sparse matrix that maps the model parameters **m** to estimates from the ambient noise surface wave and PRF estimates, **d** is the vector of observations, **L** approximates the discrete Laplacian operation via second differencing, and the subscript 2 indicates the two norm. Both the elements of **d** and associated rows of **G** were weighted by the observation reciprocal standard deviation estimates in conformance with standard (normal assumption) weighted least squares minimization. The linear system of weighted constraints was solved using LSQR [*Paige and Saunders*, 1982]. An optimal value for the trade-off parameter α of $10^{-0.93} \approx 0.12$ was determined via *L* curve analysis of seminorm value $\|\mathbf{Lm}\|_2$ versus the weighted two-norm data misfit χ^2 [e.g., *Aster et al.*, 2012, pp. 95, Figure 22].

A2. Constraint Weighting

[37] When using published PRF Moho estimates for which uncertainties were not available, 2σ standard errors were set to 2 km. In addition to a distance-to-nearest-station proportional term, an additional surface wave constraint deweighting term was included to make the edges of the model conform strongly to the smoothness constraint and thus avoid edge warping effects where constraints are exceptionally poor or absent. The surface wave model standard deviation for each model point *i* in kilometer was

$$\sigma = w_{\min}-((d_i-d_{\min})/(d_{\max}-d_{\min}))\cdot(w_{\min}-w_{\max})+20(p_i/p_{\max})^2 \quad \text{(A2)}$$

where p_i is the distance of point *i* from South Pole, $p_{\max}$ = 12,339 km is the maximum distance from the pole in the model space, d_i is the distance in km of model point *i* from the nearest seismic station (and its associated PRF Moho thickness constraint), $w_{\max}$ = 2 km, $w_{\min}$ = 18 km, $d_{\min}$ = 4.95 km, and $d_{\max}$ = 90.25 km. The resultant surface wave error surface is shown in Figure S6. Standard deviations from Table 1 and Figure S5 were applied to weight all the constraint equations in the regularized least squares problem (A1), with the relatively sparse receiver function point constraints being weighed a factor of five greater than the much denser, but less localized, surface wave constraints.

[38] **Acknowledgments.** We thank Anya Reading for helpful review comments that significantly improved this paper during revision. POLENET-ANET is supported by NSF Office of Polar Programs grants 0632230, 0632239, 0652322, 0632335, 0632136, 0632209, and 0632185. Seismic instrumentation provided and supported by the Incorporated Research Institutions for Seismology (IRIS) through the PASSCAL Instrument Center at New Mexico Tech. Seismic data are available through the IRIS Data Management Center. The facilities of the IRIS Consortium are supported by the National Science Foundation under Cooperative agreement EAR-1063471, the NSF Office of Polar Programs, and the DOE National Nuclear Security Administration. Additional information regarding the POLENET-ANET project, sites, and data is available at http://polenet.org.

References

Agostinetti, N., and A. Malinverno (2010), Receiver function inversion by trans-dimensional Monte Carlo sampling, *Geophys. J. Int.*, *181*, 858–872.

Ammon, C. J. (1991), The isolation of receiver effects from teleseismic *P* waveforms, *Bull. Seismol. Soc. Am.*, *81*, 2504–2510.

Anandakrishnan, S., and J. P. Winberry (2004), Antarctic subglacial sedimentary layer thickness from receiver function analysis, *Global Planet. Change*, *42*, 167–176.

Anthony, R. (2013), Annual and seasonal seismic background noise across Antarctica, MS Independent Study, New Mexico Institute of Mining and Technology.

Assumpcao, M., M. Feng, A. Tassara, and J. Julia (2013), Models of crustal thickness for South America from seismic refraction, receiver functions and surface wave tomography, *Tectonophysics*, *609*, 82–96.

Aster, R. C., B. Borchers, and C. Thurber (2012), *Parameter Estimation and Inverse Problems,* 2nd ed., 360 pp., Elsevier Academic Press, Waltham, Mass.

Bannister, S., R. K. Sneider, and M. L. Passier (2000), Shear-wave velocities under the Transantarctic Mountains and Terror Rift from surface wave inversion, *Geophys. Res. Lett.*, *27*(2), 281–284.

Baranov, A. A. (2010), A new crustal model for Central and Southern Asia, *Izv. Phys. Solid Earth*, *46*, 34–46.

Behrendt, J., and A. Cooper (1991), Evidence of rapid Cenozoic uplift of the shoulder escarpment of the Cenozoic West Antarctic rift system and a speculation on possible climate forcing, *Geology*, *19*, 315–319.

Behrendt, J. (1999), Crustal and lithospheric structure of the West Antarctic Rift System from geophysical investigations — A review, *Global Planet. Change*, *23*, 25–44.

Bell, R. E., D. Blankenship, C. Finn, D. Morse, T. Scambos, J. Brozena, and S. Hodge (1998), Influence of subglacial geology on the onset of a West Antarctic ice stream from aerogeophysical observations, *Nature*, *394*, 58–62.

Bentley, C. R. (1971), Seismic anisotropy in the West Antarctic ice sheet, *AGU Antarct. Res. Ser.*, *16*, 131–177.

Blankenship, D. D., R. E. Bell, S. M. Hodge, J. M. Brozena, J. C. Behrendt, and C. A. Finn (1992), Active volcanism beneath the West Antarctic ice sheet and implications for ice-sheet stability, *Nature*, *361*, 526–529.

Block, A., R. Bell, and M. Studinger (2009), Antarctic crustal thickness from satellite gravity: Implications for the Transantarctic and Gamburtsev Subglacial Mountains, *Earth Planet. Sci. Lett.*, *288*, 194–203.

Bodin, T., M. Sambridge, H. Tkalcic, P. Arroucau, K. Gallagher, and N. Rawlinson (2012), Transdimensional inversion of receiver functions and surface wave dispersion, *J. Geophys. Res.*, *117*, B02301, doi:10.1029/2011JB008560.

Bostock, M. G. (2004), Green's functions, source signatures, and the normalization of teleseismic wave fields, *J. Geophys. Res.*, *109*, B03303, doi:10.1029/2003JB002783.

Cho, T. (2011), Removing reverberation in ice sheets from receiver functions, *Seismol. Res. Lett.*, *82*, 207–210.

Clow, G., K. Cuffey, and E. Waddington (2012), High heat-flow beneath the central portion of the West Antarctic ice sheet, *Eos Trans. AGU*, Fall Meet. Suppl.

Cooper, A., F. Davey, and J. Behrendt (1987), Seismic stratigraphy and structure of the Victoria Land Basin, western Ross Sea, Antarctica, in *The Antarctic Continental Margin: Geology and Geophysics of the Western Ross Sea, CPCEMR Earth Sci. Ser.,* vol. 5B, pp. 27–76, Circum-Pac. Counc. for Energy and Miner. Resour., Houston Tex.

Cooper, A. K., and P. Barker (1995), *Geology and Seismic Stratigraphy of the Antarctic Margin, Antarct. Res. Ser.,* vol. 68, 303 pp., AGU, Washington, D. C.

Danesi, S., and A. Morelli (2001), Structure of the upper mantle under the Antarctic Plate from surface wave tomography, *Geophys. Res. Lett.*, *28*, 4395–4398.

Fretwell, P., et al. (2013), BEDMAP2: Improved ice bed, surface and thickness datasets for Antarctica, *Cryosphere*, *7*, 375–393.

Hansen, S. E., J. Julià, A. A. Nyblade, M. L. Pyle, D. A. Wiens, and S. Anandakrishnan (2009), Using S wave receiver functions to estimate crustal structure beneath ice sheets: An application to the Transantarctic Mountains and East Antarctic craton, *Geochem. Geophys. Geosyst.*, *10*, Q08014, doi:10.1029/2009GC002576.

Hansen, S. E., A. A. Nyblade, D. Heeszel, D. A. Wiens, P. Shore, and M. Kanao (2010), Crustal structure of the Gamburtsev Mountains, East Antarctica, from S-wave receiver functions and Rayleigh wave phase velocities, *Earth Planet. Sci. Lett.*, *300*, 395–401.

Hansen, S. M., K. G. Dueker, J. C. Stachnik, R. C. Aster, and K. E. Karlstrom (2013), A rootless Rockies—Support and lithospheric structure of the Colorado Rocky Mountains inferred from CREST and TA seismic data, *Geochem. Geophys. Geosyst.*, *14*, 2670–2695, doi:10.1002/ggge.20143.

Helffrich, G. (2006), Extended-time multitaper frequency domain cross-correlation receiver-function estimation, *Bull. Seismol. Soc. Am.*, *96*, 344–347.

Jordan, T. A., F. Ferraccioli, D. Vaughan, J. Holt, H. Corr, D. Blankenship, and T. Diehl (2010), Aerogravity evidence for major crustal thinning under the Pine Island Glacier region (West Antarctica), *Bull. Geol. Soc. Am.*, *122*, 714–726.

Karner, G. D., M. Studinger, and R. Bell (2005), Gravity anomalies of sedimentary basins and their mechanical implications: Application to the Ross Sea basins, West Antarctica, *Earth Planet. Sci. Lett.*, *235*, 577–596.

Kennett, B. L. N. (Compiler and Editor) (1991), *IASPEI 1991 Seismological Tables*, 167 pp., Bibliotech, Canberra, Australia.

Kohnen, H. (1974), The temperature dependence of seismic waves in ice, *J. Glaciol.*, *13*, 144–147.

Lachenbruch, A. H., and P. Morgan (1990), Continental extension, magmatism and elevation; Formal relations and rules of thumb, *Tectonophysics*, *174*, 39–62.

Lawrence, J. F., D. Wiens, A. Nyblade, S. Anandrakrishnan, P. Shore, and D. Voigt (2006), Crust and upper mantle structure of the Transantarctic Mountains and surrounding regions from receiver functions, surface waves, and gravity: Implications for uplift models, *Geochem. Geophys. Geosyst.*, *7*, Q10011, doi:10.1029/2006GC001282.

LeMasurier, W. E., and D. C. Rex (1989), Evolution of linear volcanic ranges in Marie Byrd Land, West Antarctica, *J. Geophys. Res.*, *94*, 7223–7236.

LeMasurier, W. (2008), Neogene extension and basin deepening in the West Antarctic rift inferred from comparisons with the East African rift and other analogs, *Geology*, *36*(3), 247–250.

Lindsay, J. P. (1989), The Fresnel zone and its interpretive significance, *Leading Edge*, *8*, 33–39.

Liu, Q. Y., Y. Li, J. H. Chen, R. D. van der Hilst, B. A. Guo, J. Wang, S. H. Qi, and S. C. Li (2010), Joint inversion of receiver function and ambient noise based on Bayesian theory, *Chinese J. Geophys.*, *53*, 2603–2612.

Liu, K. H., and S. S. Gao (2006), Mantle transition zone discontinuities beneath the Baikal rift and adjacent areas, *J. Geophys. Res.*, *111*, B11301, doi:10.1029/2005JB004099.

Lloyd, A., D. Wiens, A. Nyblade, S. Anandakrishnan, R. Aster, A. Huerta, T. Wilson, P. Shore, and D. Zhao (2013), Upper mantle structure beneath the Whitmore Mountains, Byrd Basin, and Marie Byrd Land from body-wave tomography, *Proc. International Symposium: Reconciling Observations and Models of Elastic and Viscoelastic Deformation due to Ice Mass Change*.

Lough, A. C., D. A. Wiens, C. G. Barcheck, S. Anandakrishnan, R. C. Aster, D. D. Blankenship, A. D. Huerta, A. Nyblade, D. A. Young, and T. J. Wilson (2013), Seismic detection of an active subglacial magmatic complex in Marie Byrd Land, Antarctica, *Nat. Geosci.*, *6*, 1031–1035, doi:10.1038/ngeo1992.

Luyendyk, B. P., C. H. Smith, and G. Druivenga (2003), Gravity measurements on King Edward VII Peninsula, Marie Byrd Land, West Antarctica, during GANOVEX VII, *Geolog. Jahrb., B*, *95*, 101–126.

McClusky, S., et al. (2010), Kinematics of the southern Red Sea–Afar Triple Junction and implications for plate dynamics, *Geophys. Res. Lett.*, *37*, L05301, doi:10.1029/2009GL041127.

Morelli, A., and S. Danesi (2004), Seismological imaging of the Antarctic continental lithosphere: A review, *Global Planet. Change*, *42*, 155–165.

Mosegaard, K., and A. Tarantola (1995), Monte Carlo methods in geophysical inverse problems, *Rev. Geophys.*, *40*, 3.1–3.29.

Paige, C. C., and M. A. Saunders (1982), LSQR: An algorithm for sparse linear equations and sparse least squares, *TOMS*, *8*(1), 43–71.

Park, J., and V. Levin (2000), Receiver functions from multiple-taper spectral correlation estimates, *Bull. Seismol. Soc. Am.*, *90*, 1507–1520.

Parker, T., B. Beaudoin, J. Gridley, and K. Anderson (2011), Next generation polar seismic instrumentation challenges, *Eos Trans. AGU*, Fall Meet. Suppl., Abstract C54B-04.

Pollard, D., R. DeConto, and A. Nyblade (2005), Sensitivity of Cenozoic Antarctic ice sheet variations to geothermal heat flux, *Global Planet. Change*, *49*(1-2), 63–74.

Pollard, D., and R. DeConto (2009), Modelling West Antarctic ice sheet growth and collapse through the past five million years, *Nature*, *458*, 329–332.

Reading, A. (2002), Antarctic seismicity and neotectonics, in *Antarctic at the Close of a Millennium,* vol. 35, pp. 479–484, R. Soc. of N. Z. Bull., New Zealand.

Reading, A. (2006), The seismic structure of Precambrian and early Palaeozoic terranes in the Lambert Glacier region, East Antarctica, *Earth Planet. Sci. Lett.*, *244*, 44–57.

Reading, A. (2007), The seismicity of the Antarctic Plate, in *Continental intraplate earthquakes: Science, hazard and policy issues*, edited by S. Stein and S. Mazzotti, *Geol. Soc. of Am. Spec. Pap.*, *425*, 285–298.

Reusch, A. M., A. A. Nyblade, M. H. Benoit, D. A. Wiens, S. Anandakrishnan, D. Voigt, and P. J. Short (2008), Mantle transition zone thickness beneath Ross Island, the Transantarctic Mountains, and East Antarctica, *Geophys. Res. Lett.*, *35*, L12301, doi:10.1029/2008GL033873.

Ritzwoller, M. H., N. Shapiro, A. Levshin, and G. Leahy (2001), The structure of the crust and upper mantle beneath Antarctica and the surrounding oceans, *J. Geophys. Res.*, *106*(B12), 30,645–30,670.

Seiberlich, C., J. Ritter, and B. Wawerzinek (2013), Topography of the lithosphere-asthenosphere boundary below the Upper Rhine Graben Rift and the volcanic Eifel region, Central Europe, *Tectonophysics*, *603*, 222–236.

Shen, W., M. Ritzwoller, V. Schulte-Pelkum, and F.-C. Lin (2012), Joint inversion of surface wave dispersion and receiver functions: A Bayesian Monte-Carlo approach, *Geophys. J. Int.*, *192*, 807–836.

Sieminski, A., E. Debayle, and J. Leveque (2003), Seismic evidence for deep low-velocity anomalies in the transition zone beneath West Antarctica, *Earth Planet. Sci. Lett.*, *216*, 645–661.

Studinger, M., R. E. Bell, W. R. Buck, G. D. Karner, and D. D. Blankenship (2004), Sub-ice geology inland of the Transantarctic Mountains in light of new aerogeophysical data, *Earth Planet. Sci. Lett.*, *220*, 391–408.

Sun, X., D. Wiens, A. Nyblade, S. Anandakrishnan, R. Aster, J. Chaput, A. Huerta, and T. Wilson (2013), Three dimensional crust and upper mantle velocity structure of Antarctica from seismic noise correlation, *Eos Trans. AGU*, Fall Meet. Suppl.

ten Brink, U. S., and M. H. Taylor (2002), Crustal structure of central Lake Baikal: Insights into intracontinental rifting, *J. Geophys. Res.*, *107*(B7), 2132, doi:10.1029/2001JB000300.

Tiberi, C., M. Diament, J. Déverchère, C. Petit-Mariani, V. Mikhailov, S. Tikhotsky, and U. Achauer (2003), Deep structure of the Baikal rift zone revealed by joint inversion of gravity and seismology, *J. Geophys. Res.*, *108*(B3), 2133, doi:10.1029/2002JB001880.

Wannamaker, P. E., J. A. Stodt, and L. Olsen (1996), Dormant state of rifting below the Byrd Subglacial Basin, West Antarctica, implied by magnetotelluric (MT) profiling, *Geophys. Res. Lett.*, *23*, 2983–2986.

Watson, T., A. Nyblade, D. A. Wiens, S. Anandakrishnan, M. Benoit, P. J. Shore, D. Voigt, and J. VanDecar (2006), P and S velocity structure of the upper mantle beneath the Transantarctic Mountains, East Antarctic craton, and Ross Sea from travel time tomography, *Geochem. Geophys. Geosyst.*, *7*, Q07005, doi:10.1029/2005GC001238.

Wiens, D., D. Heeszel, X. Sun, J. Chaput, R. Aster, A. Nyblade, T. Wilson, A. Huerta, and S. Anandakrishnan (2012), Lithospheric structure of Antarctica from Rayleigh wave tomography, *Eos Trans. AGU*, Fall Meet. Suppl.

Wiens, D., D. Heeszel, X. Sun, A. Lloyd, A. Nyblade, S. Anandakrishnan, R. Aster, J. Chaput, A. Huerta, S. Hansen, and T. Wilson (2013), Lithospheric structure of Antarctica and implications for geological and cryospheric evolution, *Proc. IASPEI Meeting*, Gothenburg, Sweden.

Wilch, T. I., D. Lux, G. Denton, and W. C. McIntosh (1993), Minimal Pliocene-Pleistocene uplift of the dry valleys sector of the Transantarctic Mountains: A key parameter in ice sheet reconstructions, *Geology*, *21*, 841–844.

Wilch, T. I., and W. C. McIntosh (2000), Eocene and Oligocene volcanism at Mount Petras, Marie Byrd Land: Implications for middle Cenozoic ice sheet reconstructions in West Antarctica, *Antarct. Sci.*, *12*(4), 477–491.

Wilson, T., et al. (2011), The POLENET Project: Data acquisition status, initial results, future modeling, *11th International Symposium on Antarctic Earth Sciences*, *Eos Trans. AGU, Fall Meet. Suppl.*, Edinburgh, Scotland, 10–16 July.

Wilson, D. S., and B. P. Luyendyk (2009), West Antarctic paleotopography estimated at the Eocene-Oligocene climate transition, *Geophys. Res. Lett.*, *36*, L16302, doi:10.1029/2009GL039297.

Wilson, D., and R. Aster (2005), Seismic imaging of the crust and upper mantle using regularized joint receiver functions, frequency–wave number filtering, and multimode Kirchhoff migration, *J. Geophys. Res.*, *110*, B05305, doi:10.1029/2004JB003430.

Winberry, J. P., and S. Anandakrishnan (2003), Seismicity and neotectonics of West Antarctica, *Geophys. Res. Lett.*, *30*, 1931–1935, doi:10.1029/2003GL018001.

Winberry, J. P., and S. Anandakrishnan (2004), Crustal structure of the West Antarctic rift system and Marie Byrd Land hotspot, *Geology*, *32*, 977–980.

Zhou, L., and H. Kanamori (2000), Moho depth variation in southern California from teleseismic receiver functions, *J. Geophys. Res.*, *105*, 2969–2980.